TiO$_2$(B)−CNT−graphene ternary composite anode material for lithium ion batteries†

Tao Shen,[ab] Xufeng Zhou,*[a] Hailiang Cao,[a] Chao Zheng[a] and Zhaoping Liu*[a]

A TiO$_2$(B)−CNT−graphene ternary composite material was prepared by *in situ* growth of TiO$_2$(B) on a conductive network composed of both graphene and CNTs. TiO$_2$(B) has nanorod morphology and is dispersed uniformly in the carbon matrices. Graphene in this composite acts as sheet-like mini-current collectors that loads TiO$_2$(B), whereas CNTs further enhance the electrical conductivity of TiO$_2$(B) by intimate contact between the two components in local regions, and also prevent the restacking between graphene layers. The composite anode material exhibits a capacity of 190 mA h g^{-1} even after 200 cycles at 1 C, presenting excellent rate performance.

Introduction

With rising interests in green electrode materials for lithium-ion batteries (LIBs), increasing attention has been paid to titanium dioxide (TiO$_2$) anode material in recent years because of its long cycle life, low cost, and minimum environmental impact.[1] However, anatase as the most widely studied polymorph of TiO$_2$ for LIBs still faces some challenges in practical applications mainly because of its low specific capacity. Luckily, TiO$_2$(B) (bronze) as a relatively new polymorph of titania is able to accommodate 1 Li$^+$ per Ti corresponding to a high theoretical capacity of 335 mA h g^{-1}.[2] TiO$_2$(B) was first synthesized in 1980 by Marchand and co-workers from the layered titanate K$_2$Ti$_4$O$_9$.[3] K$_2$Ti$_4$O$_9$ was first converted to H$_2$Ti$_4$O$_9$ *via* K$^+$/H$^+$ ion change and then calcinated to obtain TiO$_2$(B). However, the exploitation of TiO$_2$(B) as the anode material for Li-ion batteries was carried out in recent years. TiO$_2$(B) with various structures has been synthesized, aiming to improve its electrochemical performance. TiO$_2$(B) with ultra-small particle size (2.5 × 4.3 nm) was synthesized successfully by Ren *et al.*, which had higher volumetric capacity than all previously reported titania materials at rates above 1000 mA h g^{-1}.[4] Liu *et al.* prepared mesoporous TiO$_2$(B) microspheres with diameters of 1 μm, which was composed of uniform nanosized crystal grains of ∼6 nm and mesopores of 12 nm in size, and showed superior rate performance than anatase nanoparticles under the same electrode fabrication and test conditions.[5] Shin *et al.* firstly reported a facile synthetic route for preparing skein shaped TiO$_2$(B)

nanotube cluster particles with an ultra-high surface area of 257 m^2 g^{-1}, which exhibited outstanding rate capability as well as high specific capacity.[6]

It was reported that the insertion of Li ions into TiO$_2$(B) is governed by a pseudocapacitive faradaic process,[7] which results in high rate charge/discharge capabilities. However, TiO$_2$(B) still suffers from the extremely low electrical conductivity. A combination of TiO$_2$ with conducting agents, such as metals,[8] metal oxides,[9] and carbonaceous materials[10] has been proved to be an effective strategy to enhance electron transport, which also can be applied to TiO$_2$(B). Graphene nanosheet, as a new type of 2D carbon nanomaterial, can improve the electrochemical performances of various electrode materials even at a low weight fraction owing to its high intrinsic electrical conductivity, high theoretical specific surface area (2630 m^2 g^{-1}),[11] ultrathin thickness, chemical tolerance and excellent structural flexibility.[12] Huang *et al.* reported a graphene/TiO$_2$(B) hybrid with unique sheet-belt nanostructure through the hydrothermal treatment of commercial TiO$_2$ powders with graphene oxide (GO) in NaOH solution, which presented a superior rate capacity.[13] Zhang *et al.* prepared graphene-supported TiO$_2$(B) nanosheets composite, which exhibited high rate performance.[14] Vinod-kumar Etacheri *et al.* proposed a simple photocatalytic reduction method to obtain chemically bonded TiO$_2$(B) nanosheet/RGO (reduced graphene oxide) composite, and excellent capacity stability was achieved even after 1000 charge–discharge cycles at a rate of 40 C.[15] Li *et al.* introduced a simply way to fabricate TiO$_2$(B)–graphene nanoscrolls and this hybrids present good rate capability.[16] As shown in above, graphene can improve the electrical conductivity of TiO$_2$(B), and further improve the electrochemical performance. Therefore, good conductive network is the key to enhance the electrochemical performance of TiO$_2$(B). Thus, it is necessary to well design a conductive network to fully bring out the performance of TiO$_2$(B).

[a]Ningbo Institute of Materials Technology and Engineering, Chinese Academy of Sciences, Zhejiang 315201, P. R. China. E-mail: zhouxf@nimte.ac.cn; liuzp@nimte.ac.cn; Fax: +86-574-8668-5096; Tel: +86-574-8668-5096

[b]The School of Material Science and Chemical Engineering, Ningbo University, Zhejiang 315211, P. R. China
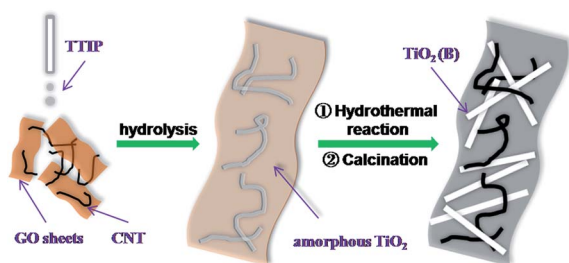
Fig. 1 Schematic illustration for the synthesis of TiO$_2$(B)–CNT–graphene composite.

In this paper, a novel TiO$_2$(B)–CNT–graphene ternary composite was designed and synthesized by an *in situ* growth procedure. The synthesis strategy for the TiO$_2$(B)–CNT–graphene composite is schematically depicted in Fig. 1. Firstly, titanium isopropoxide (TTIP) was added dropwise to the solution containing both GO and CNT. The hydrolysis of TTIP resulted in the formation of precipitation containing GO, CNT and amorphous TiO$_2$ (the TiO$_2$–CNT–GO intermediates). Following hydrothermal treatment of the precipitation in solution and subsequent calcination gave rise to the formation of ternary composites containing TiO$_2$(B) nanorods, CNT and reduced GO. In this composite, graphene sheets act as large conductive substrates, and CNTs bridge the defects for electron transfer between graphene layers and inhibit their aggregation,[17] all together to form a large and continuous conductive network. The conductive network fabricated by graphene sheets and CNTs disperses uniformly all over the composite and has intimate contact with TiO$_2$(B) nanorods, resulting in fast electron migration into the inner region of the electrode and the full access for the electrolytes into the electrode. The composites synthesized in this way delivered a higher reversible capacity and exhibited better rate performance than pure TiO$_2$(B).

Experimental

Sample preparation

GO nanosheets were prepared according to the method we reported previously.[18] CNTs were pretreated to be partially oxidized for better dispersion in water. Typically, 1 g of CNTs was pretreated in 70 ml of HNO$_3$ (68%) solution at 120 °C for 8 h. The TiO$_2$–CNT–GO intermediates were synthesized by the following procedure. A small amount of GO nanosheets and 40 mg of the pretreated CNT were dispersed in 100 ml of ethanol solution under bath ultrasonication for 30 min. Then 1.5 ml of titanium isopropoxide (TTIP) was dropwise added. After 10 min of stirring, 0.5 ml of ammonium hydroxide was added, and the mixture was kept stirring under 35 °C for 2 h. The precipitate was then collected by filtration and washed with ethanol and deionized water repeatedly. Afterwards, the TiO$_2$–CNT–GO intermediates were dispersed directly into 80 ml of 10 M NaOH aqueous solution under stirring, and then transferred into a 100 ml Teflon-coated autoclave, sealed and kept at 200 °C for 48 h. The hydrothermally treated product was dispersed in 1 M HCl solution at room temperature for 3 days. The acid solution

was renewed every 24 h. Then the product was washed with deionized water until the solution pH reached ∼7 and air-dried at 80 °C. The obtained nanocomposites were calcinated at 375 °C for 5 h, and TiO$_2$(B)–CNT–graphene nanocomposites were finally obtained and named as *i*-TBCG in the following content for convenience. For comparison, pure TiO$_2$(B) without graphene and CNT, TiO$_2$(B)/graphene composite without CNT and TiO$_2$(B)/CNT composite without graphene were also synthesized using the same procedure.

Structural characterizations

Powder X-ray diffraction (XRD) measurements were performed using an AXS D8 Advance diffractometer (Cu Kα radiation; receiving slit, 0.2 mm; scintillation counter, 40 mA; 40 kV) from Bruker Inc. The morphology and structure were analyzed by a Hitachi S-4800 field emission scanning-electron microscope (SEM) and an FEI Tecnai G2F20 transmission-electron microscope (TEM) at an accelerating voltage of 200 kV. The nitrogen sorption isotherms were recorded by a Micromeritics ASAP-2020 M nitrogen adsorption apparatus. Thermal gravimetric analysis (TGA) was performed on a Pyris Diamond thermogravimetric/differential thermal analyzer by Perkin–Elmer.

Electrochemical tests

The evaluation of electrochemical performance was carried out in CR2032-type coin cells. For the coin cells, the working electrode contained 80 wt% of active materials, 10 wt% of Super P, and 10 wt% of polyvinylidene fluoride (PVDF). The Li metal foil served as the counter electrode. The electrolyte was composed of 1 MLiPF$_6$ solution in ethylene carbonate (EC)/dimethyl carbonate (DMC) (1 : 1 by volume). The coin cells were charged/discharged within the voltage range of 0–3.0 V using a LAND-CT2001A battery test system (JinnuoWuhan Corp., China) (1 C = 300 mA g^{-1}). Electrochemical impedance spectroscopy (EIS) analysis was performed using an Autolab 83 710 electrochemical workstation. The impedance spectra were obtained by applying a sine wave. The amplitude is 5.0 mV and the frequency ranges from 100 kHz to 0.01 Hz.

Results and discussion

The TiO$_2$–CNT–GO intermediates which were synthesized by controlling the hydrolysis of TTIP are characterized by scanning electron microscopy (SEM). As shown in Fig. 2a, the intermediate composite possesses sheet-like morphology, similar as graphene. CNTs can also be seen on graphene layers owing to the π–π stacking interaction between CNTs and graphene[17] and TiO$_2$ grown between them, which is more obvious in the high-magnification SEM image (Fig. 2b). The corresponding EDX maps show homogeneous distribution of Ti, O and C in the sample, proving that the TiO$_2$ was distributed uniformly on the carbon materials. For comparison, the structure of CNT–graphene composite without adding TTIP was also investigated. As shown in Fig. S1,† CNTs are randomly and uniformly distributed on the surface of GO sheets. Two components stick with each other strongly due to the π–π interaction between
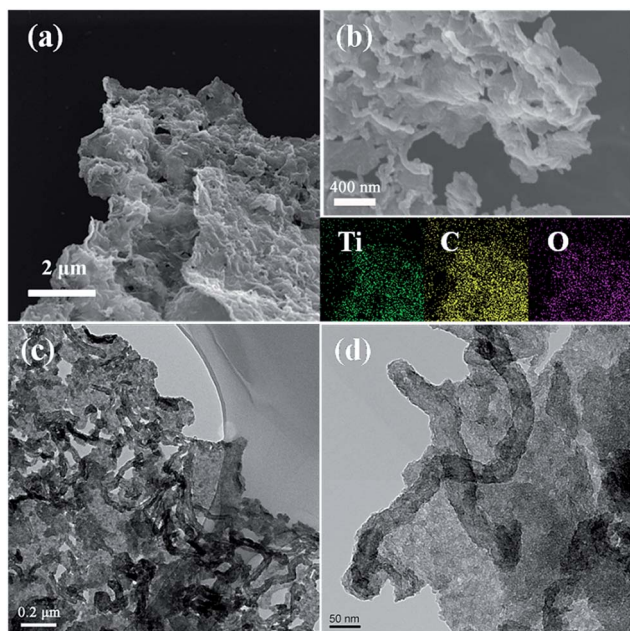
Fig. 2 (a) Low-magnification SEM image and corresponding EDX maps, (b) high-magnification SEM image, (c) low-magnification TEM image and (d) high-magnification TEM image for the TiO$_2$–CNT–GO intermediates obtained by freeze drying.

them. The XRD pattern (blue curve in Fig. 3) shows the amorphous nature of TiO$_2$ species in the intermediate product. The structure of the intermediates is further investigated by transmission electron microscope (TEM). Fig. 2c presents the low-magnification TEM image of the TiO$_2$–CNT–GO intermediates. The sheet-like structure can be seen, which is consistent with the SEM image. Comparing to GO, the transparency of the intermediates under electron beam is obviously lower, indicating that the thickness increases significantly. Meanwhile, some fibrous materials can be observed in the intermediates, which can be recognized as the CNTs. Zooming-in further, as shown in Fig. 2d, a layer of amorphous materials distribute
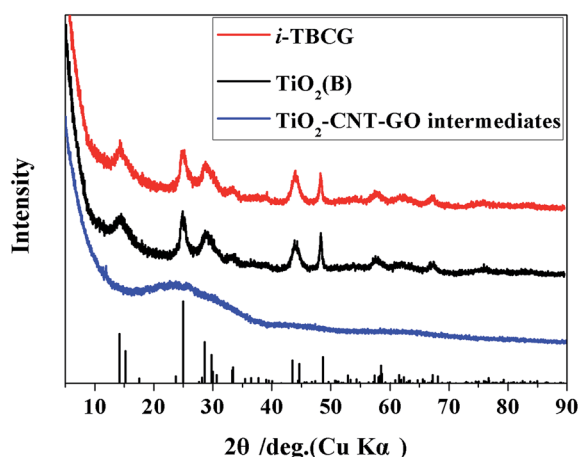
uniformly in the sample, which is amorphous TiO$_2$. The tubular structure of CNTs is clearly visible under the high-magnification TEM, however, the surface is obviously rougher than pure CNTs, which is due to the formation of amorphous TiO$_2$ on the surface of CNTs. Therefore, it can be deduced that GO and the treated CNTs, both of which have plenty of oxygen-containing functional groups, have strong interaction with the hydrolysis products of TTIP that are rich in hydroxyl, leading to the uniform attachment of amorphous TiO$_2$ on the surface of GO and CNTs, to form the intermediates with sheet-like morphology.

After the hydrothermal procedure and the calcination treatment, the amorphous TiO$_2$ turns into TiO$_2$(B) which is crystalline and the TiO$_2$–CNT–GO intermediates are transformed to the i-TBCG. Fig. 3 shows the XRD patterns of the obtained samples. The red curve refers to i-TBCG. The lattice parameters calculated from the XRD pattern ($a = 12.179$ Å, $b = 3.741$ Å, $c = 6.525$ Å, and $\theta = 107.05°$) match well with TiO$_2$(B) (JCPDS 74-1940), exhibiting a typical TiO$_2$(B) (bronze) structure. The black curve refers to the pure TiO$_2$ (B) synthesized using the similar procedure as i-TBCG, but without adding GO and CNT, which is almost identical to the pattern for i-TBCG.

The SEM images of the i-TBCG are displayed in Fig. 4. As shown in Fig. 4a, a large number of TiO$_2$(B) nanorods with a few micrometers in length are loaded on graphene sheets. Fig. 4b displays the SEM image of i-TBCG with a higher magnification. Some parts of TiO$_2$(B) nanorods are intimately attached to graphene sheets, suggesting strong interaction between two components. It is difficult to distinguish CNTs from TiO$_2$(B) nanorods in the SEM images due to similar size and morphology between two components. To further examine the
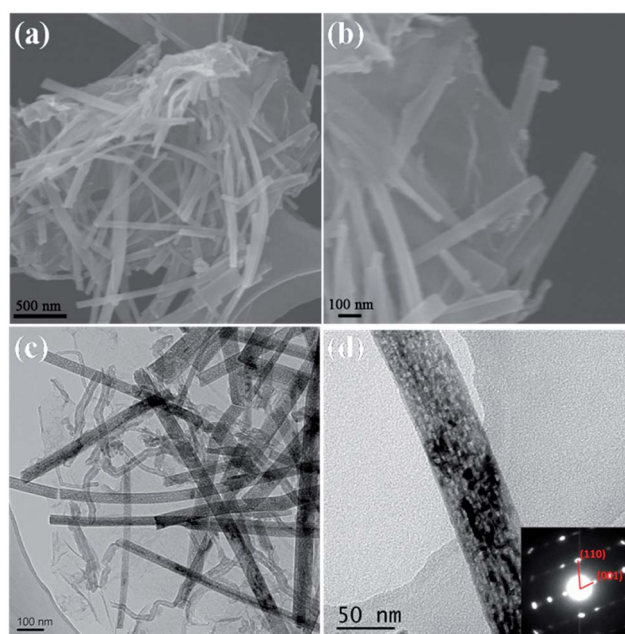

Fig. 4 (a) Low-magnification SEM image, (b) high-magnification SEM image and (c) low-magnification TEM image of i-TBCG and (d) high-magnification TEM image of an individual TiO$_2$(B) nanorod in i-TBCG. The inset in (d) is the corresponding SAED pattern.

Fig. 3 XRD patterns of the TiO$_2$–CNT–GO intermediates, TiO$_2$ (B) and i-TBCG.

structure of this composite, the samples were investigated by TEM. Fig. 4c presents the typical TEM image of the *i*-TBCG. Graphene sheets show a thin film-like structure in this image, which is almost transparent under TEM. $TiO_2(B)$ nanorods with several micrometers in length and 50–100 nanometers in width lay randomly on the surface of graphene sheets. CNTs can also be observed on graphene sheets, which interwine with TiO_2 nanorods. In this structure, graphene sheets act as conductive substrates to support TiO_2, whereas CNTs further enhance the conductivity by intimate contact with TiO_2 nanorods. Fig. 4d shows the high-magnification TEM image of one $TiO_2(B)$ nanorod. Some rectangular pores can be observed from the surface of the $TiO_2(B)$ nanorods, which is similar to the sample reported previously.[13] The SAED pattern indicates the single crystal nature of the nanorod, and can be indexed as the $TiO_2(B)$ structure, in good accordance with the XRD results, and the crystal parameters calculated from the SAED pattern also match well with the XRD data.

As shown in Fig. 5a, the Brunauer–Emmett–Teller (BET) specific surface area of pure $TiO_2(B)$ and *i*-TBCG is also investigated by nitrogen sorption, which is calculated to be 32.2 and 65.5 m^2 g^{-1}, respectively. The larger BET specific surface area for *i*-TBCG is probably attributed to the presence of graphene sheets and CNTs. The $TiO_2(B)$ sample has a broad pore size distribution centered at ∼80 nm, which can be ascribed to the interparticle space of randomly stacked $TiO_2(B)$ nanorods. Fig. 5b presents the TG measurement of pure $TiO_2(B)$ and *i*-TBCG. It can be seen that the carbon materials decomposes thoroughly at 700 °C. The weight retention of *i*-TBCG and pure $TiO_2(B)$ is measured to be 86.3% and 97.3%, respectively, so the weight percentage of carbon materials (including graphene and CNTs) is estimated to be 11.2 wt%. To further differentiate the weight content of graphene and CNTs, TG measurement of $TiO_2(B)$/graphene composite without CNTs was carried and the result is shown in Fig. S3.† The weight loss for $TiO_2(B)$/graphene is 4.3%. It then can been calculated that the weight percent of graphene and CNT in *i*-TBCG are 1.6 and 9.6%, respectively.

Fig. 6a exhibits the first galvanostatic discharge/charge curves of $TiO_2(B)$ and *i*-TBCG at 0.1 C. The coulombic efficiency of $TiO_2(B)$ and *i*-TBCG are 53.2% and 50.5%, respectively.

The irreversible capacity loss in the first cycle mainly arises from reactions between the surface of $TiO_2(B)$ and the electrolyte.[19] The higher irreversible capacity loss of *i*-TBCG is probably due to the irreversible reactions between Li^+ and graphene sheet.[20] The capacity of $TiO_2(B)$ in the first galvanostatic discharge curve is 493.7 mA h g^{-1}, which is higher than the theoretical capacity of $TiO_2(B)$. The extra capacity is probably caused by the side reaction of $TiO_2(B)$ and the electrolyte. The capacity of *i*-TBCG is even higher than that of pure $TiO_2(B)$, which can be attributed to the synergetic effect of graphene and CNTs. We can see from Fig. 6b that the capacity of $TiO_2(B)$ and *i*-TBCG is 272 and 388 mA h g^{-1} respectively in the second cycle at the rate of 0.1 C. With the relatively low content of carbon materials the capacity of *i*-TBCG increases by 42% comparing with that of $TiO_2(B)$. It is the conductive network fabricated by graphene sheets and CNTs that releases the possible capacity of $TiO_2(B)$.

Fig. 6b presents the rate capability of two anode materials tested from 0.1 to 10 C. The significant irreversible capacity loss upon first discharge for both samples can also be found in Fig. 6b. It can be seen that *i*-TBCG shows apparent advantage over pure $TiO_2(B)$ in the term of capacity throughout the whole test. At a high rate of 10 C, the discharge capacities of *i*-TBCG and pure $TiO_2(B)$ reach 75.9 and 5.8 mA h g^{-1}, respectively. *i*-TBCG also shows better rate performance comparing with $TiO_2(B)$–graphene composite anode materials reported previously.[16,21] It may owe to the uniform dispersion of $TiO_2(B)$ nanorods in *i*-TBCG and a continuous conductive network formed by both graphene sheets and CNTs. The electrochemical performance of graphene and CNTs were also tested as shown in Fig. S4 and S5.† Though both graphene and CNT have electrochemical activity within the voltage range of 0.01–3 V, their capacity contribution in *i*-TBCG should be limited due to their low weight content (totally 11.2 wt%) in the ternary composite. The main function of graphene and CNTs in *i*-TBCG is to fabricate a conductive network to enhance the electrochemical performance of $TiO_2(B)$. After the high rate test, the cells were remeasured at a relatively low rate of 1 C again. It is surprising to note that the capacities of the two anode materials both exceed the ones measured during the initial 1 C cycles. This
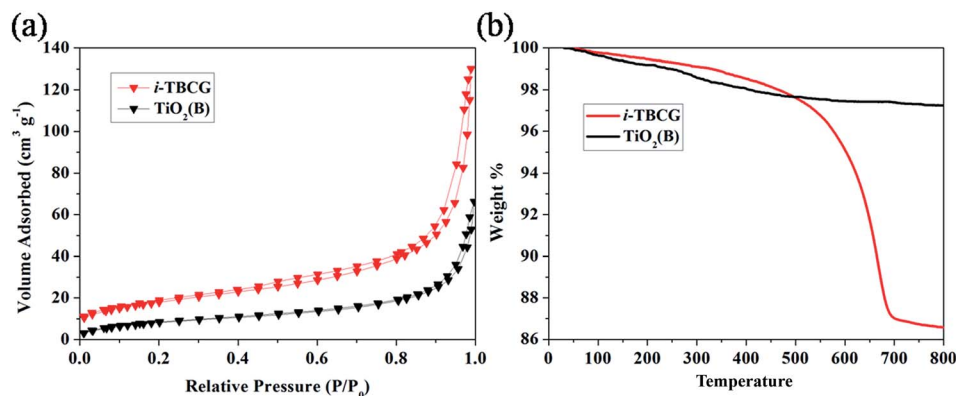

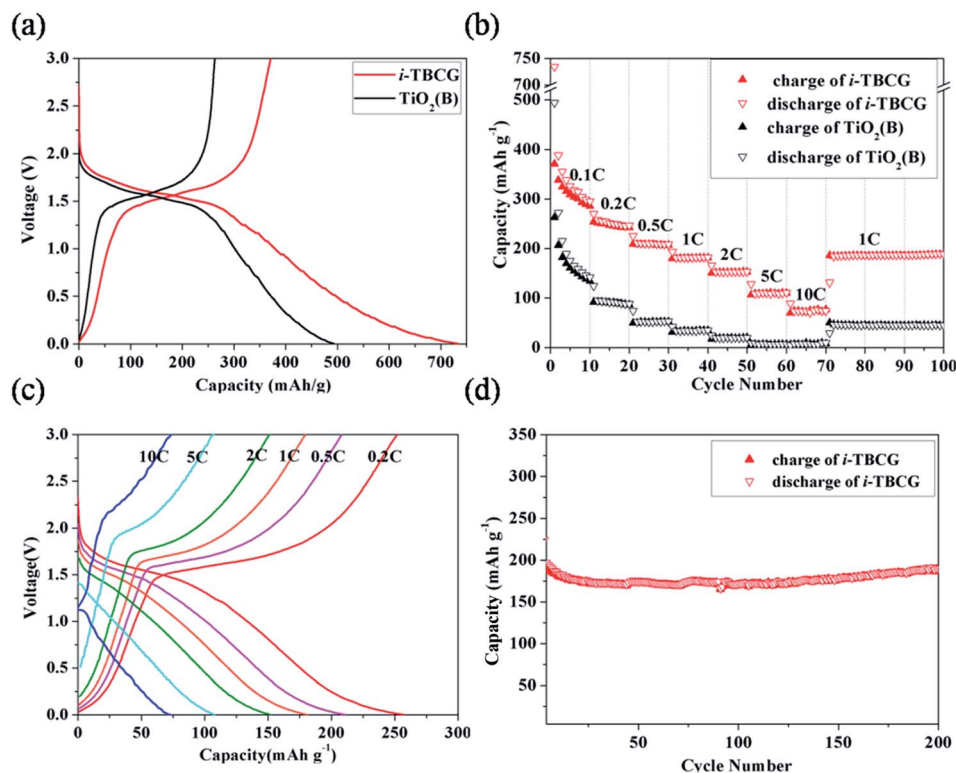Fig. 5 (a) Nitrogen adsorption−desorption isotherms and (b) thermogravimetric analysis of $TiO_2(B)$ and *i*-TBCG.

Fig. 6 (a) Curves for the initial galvanostatic discharge/charge of $TiO_2(B)$, and *i*-TBCG at 0.1 C, (b) the plot of specific capacity *vs.* charge/discharge rates for $TiO_2(B)$ and *i*-TBCG. (c) Curves for galvanostatic discharge/charge of *i*-TBCG at different rates, (d) the cyclic curve of *i*-TBCG at 1 C for 200 cycles.

phenomenon has been observed in TiO_2 anode materials,[10a] which was ascribed to the activation process of the electrode materials during cycling. To further verify the effect of the conductive network composed by both graphene and CNTs in *i*-TBCG, the electrochemical performance of $TiO_2(B)$/graphene composite and $TiO_2(B)$/CNTs composite were tested. As shown in Fig. S6 and S7,† their rate performance is apparently worse than that of *i*-TBCG, suggesting the synergetic effect of graphene and CNTs in improving the electrochemical performance of *i*-TBCG.

Fig. 6c shows the typical curves for galvanostatic discharge/charge of *i*-TBCG at different rates. As the rate increases, the gradient of the discharge curve increases, and the voltage gap between the charge and discharge curves also increases, indicating raised polarization at high rates. Fig. 6d exhibits the cycling tests of *i*-TBCG at 1 C for 200 cycles (except the first two cycles). The specific discharge capacity of *i*-TBCG is 190 mA h g^{-1} at the 200th cycle, which still retains 96% of its initial discharge capacity, showing excellent cycling stability.

In order to investigate the rate performance of the two anode materials further, Nyquist plots are measured after the rate tests. Circle arc in the high frequency region and the sloping straight line in the low frequency region is basically related to the transportation of electron and lithium ion in the active material, respectively.[22] As exhibited in Fig. 7, *i*-TBCG has smaller circle arc in the high frequency region and larger gradient of the sloping straight line in the low frequency region
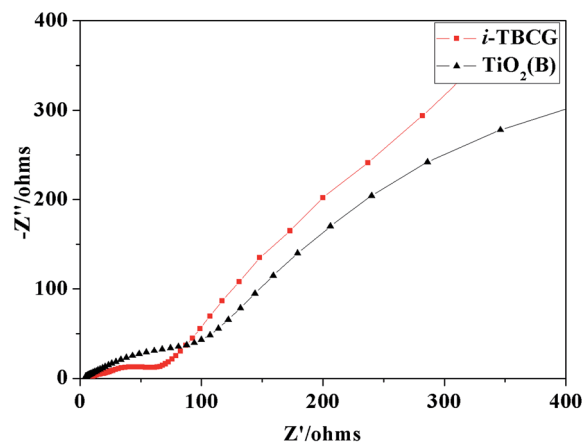

Fig. 7 Nyquist plots of *i*-TBCG and $TiO_2(B)$.

comparing with those of pure $TiO_2(B)$, implying better rate performance than that of pure $TiO_2(B)$, which agrees with the rate capability tests.

Conclusions

The $TiO_2(B)$–CNT–graphene ternary composite was synthesized through *in situ* growth procedure, in which $TiO_2(B)$ was uniformly distributed on the conductive network composed by both graphene and CNTs. The *i*-TBCG composites show better

rate performance and better cycle stability than pure $TiO_2(B)$. The conductive network constructed by both graphene sheets and CNTs contributes to the excellent electrochemical performance of this anode material. It is believed that the conductive network fabricated by the carbon materials can also been applied to other anode materials with low conductivity, thus to produce series of high-performance electrode materials.

Acknowledgements

References

1 X. B. Chen and S. S. Mao, *Chem. Rev.*, 2007, **107**, 2891.

2 A. G. Dylla, G. Henkelman and K. J. Stevenson, *Acc. Chem. Res.*, 2013, **46**, 1104.

3 R. Marchand, L. Brohan and M. Tournoux, *Mater. Res. Bull.*, 1980, **15**, 1129.

4 Y. Ren, Z. Liu, F. Pourpoint, A. R. Armstrong, C. P. Grey and P. G. Bruce, *Angew. Chem., Int. Ed.*, 2012, **51**, 2164.

5 H. S. Liu, Z. H. Bi, X. G. Sun, R. R. Unocic, M. P. Paranthaman, S. Dai and G. M. Brown, *Adv. Mater.*, 2011, **23**, 3450.

6 K. Shin, H. J. Kim, J. M. Choi, Y. M. Choi, M. S. Song and J. H. Park, *Chem. Commun.*, 2013, **49**, 2326.

7 M. Zukalová, M. Kalbáč, L. Kavan, I. Exnar and M. Graetzel, *Chem. Mater.*, 2005, **17**, 1248.

8 W. Wang, M. Tian, A. Abdulagatov, S. M. George, Y. C. Lee and R. G. Yang, *Nano Lett.*, 2012, **12**, 655.

9 (*a*) Y. S. Luo, J. S. Luo, J. Jiang, W. W. Zhou, H. P. Yang, X. Y. Qi, H. Zhang, H. J. Fan, D. Y. W. Yu, C. M. Li and T. Yu, *Energy Environ. Sci.*, 2012, **5**, 6559; (*b*) K. S. Park, J. G. Kang, Y. J. Choi, S. Lee, D. W. Kim and J. G. Park, *Energy Environ. Sci.*, 2011, **4**, 1796.

10 (*a*) X. Xin, X. F. Zhou, J. H. Wu, X. Y. Yao and Z. P. Liu, *ACS Nano*, 2012, **6**, 11035; (*b*) Y. G. Guo, Y. S. Hu, W. Sigle and J. Maier, *Adv. Mater.*, 2007, **19**, 2087.

11 J. C. Meyer, A. K. Geim, M. I. Katsnelson, K. S. Novoselov, T. J. Booth and S. Roth, *Nature*, 2007, **446**, 60.

12 P. V. Kamat, *J. Phys. Chem. Lett.*, 2011, **2**, 242.

13 H. Huang, J. W. Fang, Y. Xia, X. Y. Tao, Y. P. Gan, J. Du, W. J. Zhu and W. K. Zhang, *J. Mater. Chem. A*, 2013, **1**, 2495.

14 Z. Zhang, Q. X. Chu, H. Y. Li, J. H. Hao, W. S. Yang, B. P. Lu, X. Ke, J. Li and J. L. Tang, *J. Colloid Interface Sci.*, 2013, **409**, 38.

15 V. Etacheri, J. E. Yourey and B. M. Bartlett, *ACS Nano*, 2014, **8**, 1491.

16 X. Li, Y. Zhang, T. Li, Q. Zhong, H. Li and J. Huang, *J. Power Sources*, 2014, **268**, 372.

17 L. Shen, X. Zhang, H. Li, C. Yuan and G. Cao, *J. Phys. Chem. Lett.*, 2011, **2**, 3096.

18 X. F. Zhou and Z. P. Liu, *Chem. Commun.*, 2010, **46**, 2611.

19 S. Brutti, V. Gentili, H. Menard, B. Scrosati and P. G. Bruce, *Adv. Energy Mater.*, 2012, **2**, 322.

20 H. L. Wang, L. F. Cui, Y. A. Yang, H. S. Casalongue, J. T. Robinson, Y. Y. Liang, Y. Cui and H. J. Dai, *J. Am. Chem. Soc.*, 2010, **132**, 13978.

21 (*a*) X. Li, Y. Zhang, Q. Zhong, T. Li, H. Li and J. Huang, *Appl. Surf. Sci.*, 2014, **313**, 877; (*b*) J. Hou, R. Wu, P. J. Zhao, A. M. Chang, G. Ji, B. Gao and Q. Zhao, *Mater. Lett.*, 2013, **100**, 173.

22 Q. Zhang, S. Xu, X. Qiu, Y. Cui, L. Fang and S. Sun, *Progr. Chem.*, 2010, **22**, 1044.